ADVANCED MATERIALS TECHNOLOGIES
www.advmattechnol.de



# Leveraging Monostable and Bistable Pre-Curved Bilayer Actuators for High-Performance Multitask Soft Robots

*Yinding Chi, Yichao Tang, Haijun Liu, and Jie Yin**

**Soft actuators are typically designed to be inherently stress-free and stable. Relaxing such a design constraint allows exploration of harnessing mechanical prestress and elastic instability to achieve potential high-performance soft robots. Here, the strategy of prestrain relaxation is leveraged to design pre-curved soft actuators in 2D and 3D with tunable monostability and bistability that can be implemented for multifunctional soft robotics. By bonding stress-free active layer with embedded pneumatic channels to a uniaxially or biaxially pre-stretched elastomeric strip or disk, pre-curved 2D beam-like bending actuators and 3D doming actuators are generated after prestrain release, respectively. Such pre-curved soft actuators exhibit tunable monostable and bistable behavior under actuation by simply manipulating the prestrain and the biased bilayer thickness ratio. Their implications in multifunctional soft robotics are demonstrated in achieving high performance in manipulation and locomotion, including energy-efficient soft gripper to holding objects through prestress, fast-speed larva-like jumping soft crawler with average locomotion speed of 0.65 body-length $s^{-1}$ (51.4 mm $s^{-1}$), and fast swimming bistable jellyfish-like soft robot with an average speed of 53.3 mm $s^{-1}$.**

## 1. Introduction

Soft robot made of entirely soft materials has recently attracted increasing research interest due to its potentially infinite degree of freedom, high compatibility, super adaptivity, and safe interaction with environments.[1] The robotic functions in locomotion and manipulation are achieved by continuously deforming its soft body through extension/contraction, bending, and torsion under actuation. Among them, a bilayer structural design composed of one active layer and one passive strain-limiting layer is often employed to construct its soft body due to its simplicity in both deformation control and fabrication.[2] Under actuation, a mechanical strain mismatch will develop between the bilayer to bend or twist the soft body. Such a bilayer soft actuator has been widely used in the design of micro-robots,[3] artificial muscle,[4] bio-mimic robots,[5] and medical rehabilitation.[6]

However, most of these soft bilayer actuators employ an initial stress-free and planar configuration, which is inherently designed to be stable. Thus, it precludes the potential instability or bistability that often requires a pre-curved shape to switch between two stable states. Very recently, bistability has been harnessed in soft robots for untethered directional propulsion,[7] autonomous control of airflow in soft bistable valves,[8] soft fluidic actuators with amplified responses,[9] and cheetah-like galloping soft robots,[10] demonstrating its power in enhancing diverse high-performance functionalities in soft robots.

Here, we utilize the strategy of pre-stretching-induced mismatch strain in a homogeneous bilayer system to generate pre-stressed and pre-curved soft bilayer actuators in 2D and 3D. The soft actuator takes the form of both a 2D bent beam-like shape and a 3D dome shape. Such a prestrain release strategy has been widely used in designing stretchable electronics[11] and self-assembly of 3D structures from 2D sheets and stripes at all scales through buckling.[12] Very recently, it has been applied to fabricate 3D elastomeric structures[13] and bio-inspired fast-response soft machines from 2D pre-strained bi-strips.[14] However, most of these fabricated 3D structures are stable, exhibiting monotonic bending behavior under actuation. Our recent study of LEAP soft robots demonstrated leveraging the strategy of tunable monostable and bistable mechanism for high-speed locomotion and high-strength manipulation.[10] It features a hybrid design of integrating a rigid bistable spine with 2D soft bending actuators. However, how to extend a similar strategy to design high-performance entirely soft robotics without a rigid bistable spine remains largely unexplored. In this work, by replacing the bistable spine with a pre-stretched spineless soft bilayer system, we show that the stability of entirely soft pre-curved 2D and 3D actuators can be tuned from monostable to bistable by simply manipulating the bilayer thickness ratio and prestrain. As the actuation input increases, the pre-curved actuators are demonstrated to either bend further to increase their bending curvature or flip their bending directions to generate a negative bending curvature. Last, we demonstrate utilizing monostable and bistable bilayer actuators for

Y. Chi, Dr. Y. Tang, Prof. J. Yin
Department of Mechanical and Aerospace Engineering
North Carolina State University
Raleigh, NC 27695, USA
E-mail: jyin8@ncsu.edu
Prof. H. Liu
Department of Mechanical Engineering
Temple University
Philadelphia, PA 19122, USA
The ORCID identification number(s) for the author(s) of this article can be found under https://doi.org/10.1002/admt.202000370.

DOI: 10.1002/admt.202000370

 

designing a variety of high-performance soft robots, including an energy-efficient pre-stressed soft gripper, a fast-moving pre-curved soft crawler, and a fast-speed bistable jelly-fish-like soft swimmer.

## 2. Results and Discussions

### 2.1. Design of 2D and 3D Pre-Curved Soft Bilayer Actuators

**Figure 1**a,b shows the schematics of fabricating two representative pre-curved bilayer actuators in 2D and 3D through the prestrain release strategy, respectively. A beam-like elastomeric strip (denoted in green color) with length of $L_o$ (Figure 1a (i)) is first uniaxially pre-stretched to length $L = (1 + \varepsilon_{pre})\ L_o$ with $\varepsilon_{pre}$ being the prestrain, followed by bonding a stress-free layer with embedded zig-zag pneumatic channels on the top with the same length of $L$ (denoted in blue color, Figure 1a (ii); Figure S1a, Supporting Information; see Experimental Section for more details). Both layers are made of the same elastomeric materials (Ecoflex 00–50, Smooth-on Inc.) to form a homogeneous bilayer structure. After releasing the prestrain in the pre-stretched bottom layer, it bends downward and forms a pre-stressed concave arc-shaped soft bending actuator (Figure 1a (iii)). Similarly, by bonding a stress-free pneumatic layer on top of an equi-biaxially pre-stretched circular elastomeric plate along the radial direction (Figure 1b (i,ii)), it generates a pre-stressed concave dome-shaped soft bending actuator in 3D upon prestrain release (Figure 1b (iii)), where a patterned spiral pneumatic channel is employed for isometric doming deformation under pressurization[5c] (Figure S1b, Supporting Information).

Upon inflating the pre-curved soft actuators, they can demonstrate distinct bending behavior by manipulating the thickness ratio of the pre-stretched bottom layer $h_b$ underneath the channel and the initial stress-free top layer $h_t$ above the channel (Figure 1a (iv-v),b(iv-v)). For both 2D beam-like and 3D dome-like soft bending actuators, when $h_b > h_t$, i.e., actuators with a relatively thick pre-stretched layer, they can further bend downward with an increased positive bending curvature (Figure 1a (iv),b(iv)). In contrast, when $h_b < h_t$, i.e., actuators with a relatively thin pre-stretched layer, their bending directions can flip to bend upward with a negative bending curvature (Figure 1a (v),b(v)), demonstrating potential tunable monostability and bistability as discussed later. To simplify the comparison of different bilayer thickness ratios in 2D and 3D soft actuators, the channel height $h_c$ and their total thickness $h = h_t + h_c + h_b$ are kept the same. Without loss of generality, simply switching the value of $h_t$ and $h_b$ in the system renders two counterparts for comparison: one has a thicker pre-stretched layer with $h_b/h_t = r > 1$ and the other has a thinner pre-stretched layer with $h_b/h_t = 1/r < 1$. In the following, we will discuss how the thickness ratio and prestrain affect their pre-curved shapes before actuation and their tunable monostable/bistable bending behavior in both 2D and 3D bending actuators upon actuation, respectively.

### 2.2. 2D Arched Soft Bending Actuators

#### *2.2.1. Pre-Curved Shapes After Uniaxial Prestrain Release*

**Figure 2**a shows the comparison of the bent shapes between homogenous soft bending actuators with a thicker pre-stretched layer on the bottom ($h_b/h_t = 10/3 > 1$ with $h_b = 5$ mm and $h_t = 1.5$ mm, left) and their counterparts by switching their top and bottom layer thickness ($h_b/h_t = 3/10 < 1$ with $h_b = 1.\ 5$ mm and $h_t = 5$ mm, right) after the release of different prestrains

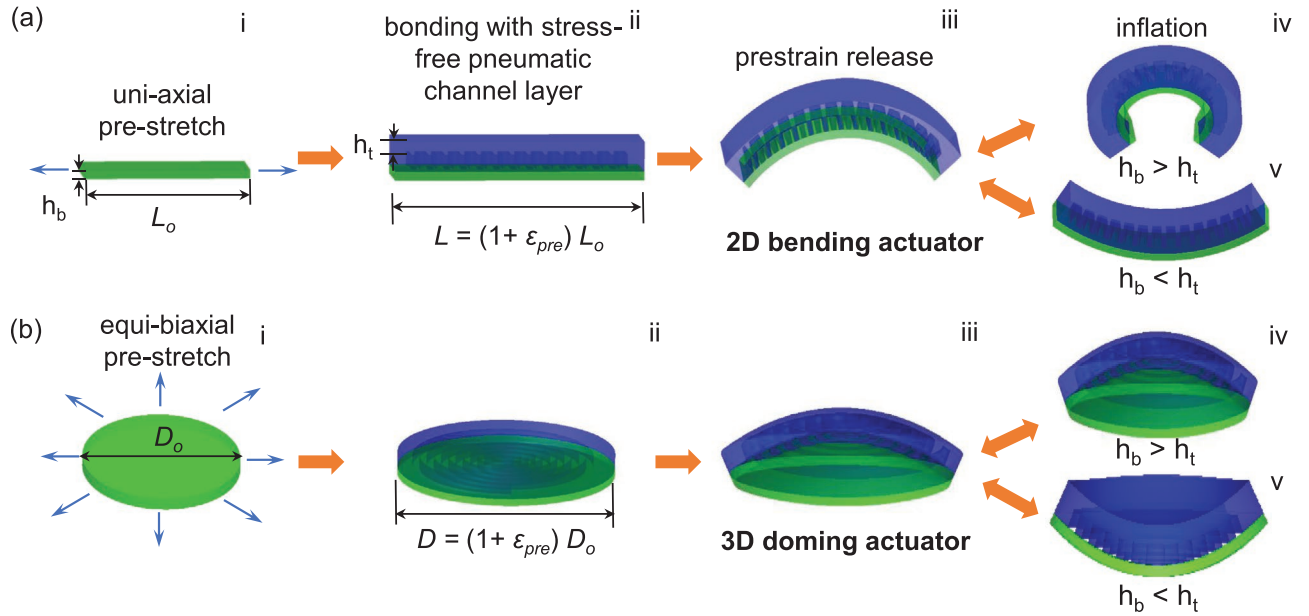


**Figure 1.** a,b) Schematic illustration of fabricating pre-curved 2D (a) and 3D soft bilayer actuators (b) through prestrain-release strategy. A strip or circular disk is first uni-axially or equi-biaxially pre-stretched (i), then bonding to a stress-free pneumatic channel layer on the top (ii). Release of the prestrain leads to pre-curved 2D beam-like bending actuator and 3D doming actuators (iii). Upon inflation in the air channel, it can either further bend or dome for actuators with a thicker pre-stretched layer (iv), or flip to the opposite direction for actuators with a thinner pre-stretched layer (v).

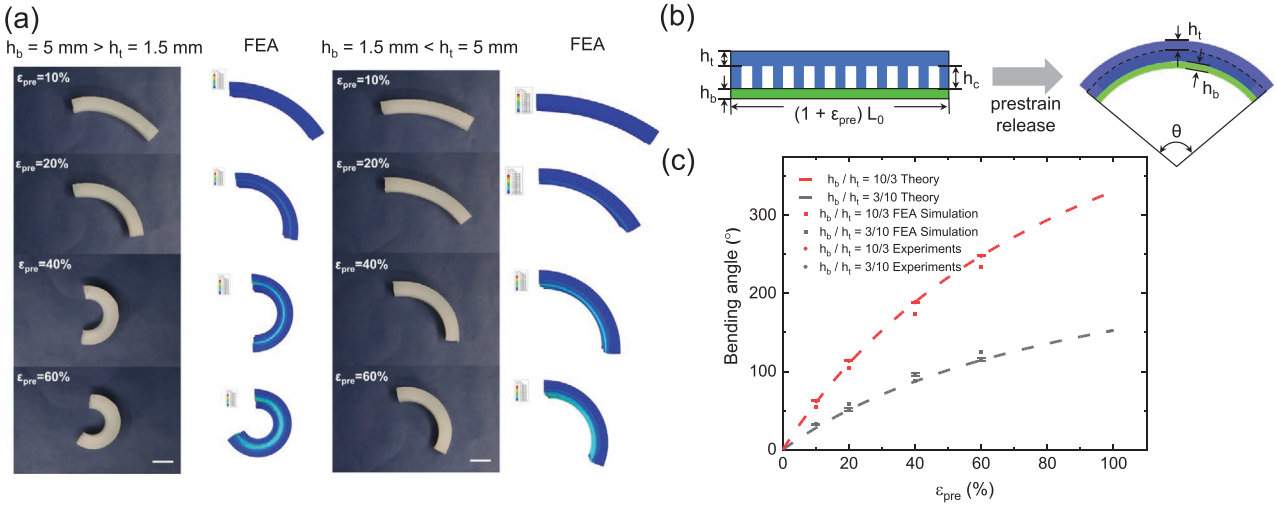


**Figure 2.** a) Comparison of pre-curved 2D soft bilayer bending actuators and their counterparts with stress-free top layer thickness ($h_t$) and pre-stretched bottom layer thickness ($h_b$) switched after different prestrain $\varepsilon_{pre}$ release. Corresponding FEA simulation results of Mises stress contour are shown to the right. b) Schematic of bending of bilayer strip with pneumatic channels after prestrain release. c) Comparison of bending angle versus prestrain $\varepsilon_{pre}$ between experiments, theory, and FEA for 2D bending actuators with different bilayer thickness ratio $h_b/h_t$ (scale bar: 10 mm)

$\varepsilon_{pre}$, where $h_c$ = 5 mm and $h$ = 11.5 mm are kept the same (Figure 2b). It shows that after the prestrain release, both cases of actuators bend toward the pre-strained bottom layer and their bending angles $\theta$ (defined in Figure 2b) and bending curvatures increase with $\varepsilon_{pre}$. The corresponding experimental data on $\theta$ versus $\varepsilon_{pre}$ are shown in Figure 2c. It shows that $\theta$ increases monotonically and nonlinearly with $\varepsilon_{pre}$, which is consistent with previous studies on the bistrip soft actuators.[13–14] At the same applied $\varepsilon_{pre}$, the actuators with a thicker pre-stretched layer exhibit a larger bending angle than their counterparts due to their lower bending stiffness resistance of thin top layer. The disparity of $\theta$ between two counterparts increases dramatically with $\varepsilon_{pre}$ (Figure 2c), showing a dominant role of the bilayer thickness ratio $h_b/h_t$ in manipulating the shape of pre-curved 2D bending actuators. Specifically, at $\varepsilon_{pre}$ = 40%, the actuator with a thicker pre-stretched layer bends into a half-circle with $\theta \approx 180^o$, which approximately doubles the bending angle of its counterpart. As $\varepsilon_{pre}$ further increases, it can even bend beyond 180° tending to be closed. As shown in Figure 2a,c, the corresponding finite element analysis (FEA) simulation results (see Experimental Section for details) on bending of both types of actuators show an excellent agreement with the experiments.

The bending angle $\theta$ in both cases of prestrained actuators as a function of prestrain can be well predicted by the classical bistrip bending model under mismatch strain,[15] which gives:

$$\theta = \frac{180^o}{\pi}\frac{L}{h}\frac{6(1+m)^2}{\left[3(1+m)^2+(1+mn)\left(m^2+1/mn\right)\right]}\frac{\varepsilon_{pre}}{(1+\varepsilon_{pre})} \quad (1)$$

where $m = (h_t + h_c)/h_b$ and $n = E_t/E_b$ are the thickness ratio and Young's modulus ratio of the stress-free top layer and pre-stretched bottom layer, respectively. The stress-free top layer includes both the channeled layer and the layer on top of the channel. $\varepsilon_{pre}/(1+\varepsilon_{pre})$ is the mismatched strain between the two layers. $L$ is the length of the stress-free top layer, i.e., the length of the actuator. We assume that $L$ does not change after the prestrain release. Considering the small size of the channels, the effect of the channeled structure on the bending stiffness of the actuator can be neglected in the above model. Thus, we have $n = 1$ in Equation (1) and assume a simplified linear elastic model of the elastomer without considering materials nonlinearity. Equation (1) shows that the bilayer bending actuator will always take an initial pre-bended shape with nonzero $\theta$ when $\varepsilon_{pre} \neq 0$, i.e., the only scenario for a straight configuration is that there is no mismatch strain with $\varepsilon_{pre} = 0$. Figure 2c shows that the simplified model agrees well with both experiments and FEA simulation results for both cases of pre-stressed actuators, which validate the model.

### 2.2.2. Bending Behavior Under Actuation

Upon inflating the air channel, **Figure 3**a,b shows that the two pre-curved actuators with switched bilayer thickness exhibit opposite bending directions. For the actuator with a thicker bottom pre-stretched layer, i.e., $h_b > h_t$, as the air pressure $p$ increases from 0 to 30 kPa, it bends downward (positive bending angle $\theta$) further due to the expansion of the thinner top layer, and forms a closed ring shape (Figure 3a). In contrast, for its counterpart with switched top and bottom layer thickness ($h_b < h_t$), it bends upward to be away from its center due to the expansion of the thinner bottom pre-stretched layer, and forms a half-circular shape at $p$ = 30 kPa with its bending direction flipped (negative $\theta$; Figure 3b). This is in sharp contrast to the actuated monotonic bending of pre-strained soft actuators without changing their bending directions reported in previous studies.[13–14] The switch from monotonic positive bending to flip to negative curvature with the increase of $p$ are well captured by the corresponding FEA simulations (Figure 3a,b, right).

Figure 3c,d shows the measured bending angles $\theta$ as a function of $p$ for both pre-curved actuators with different prestrains

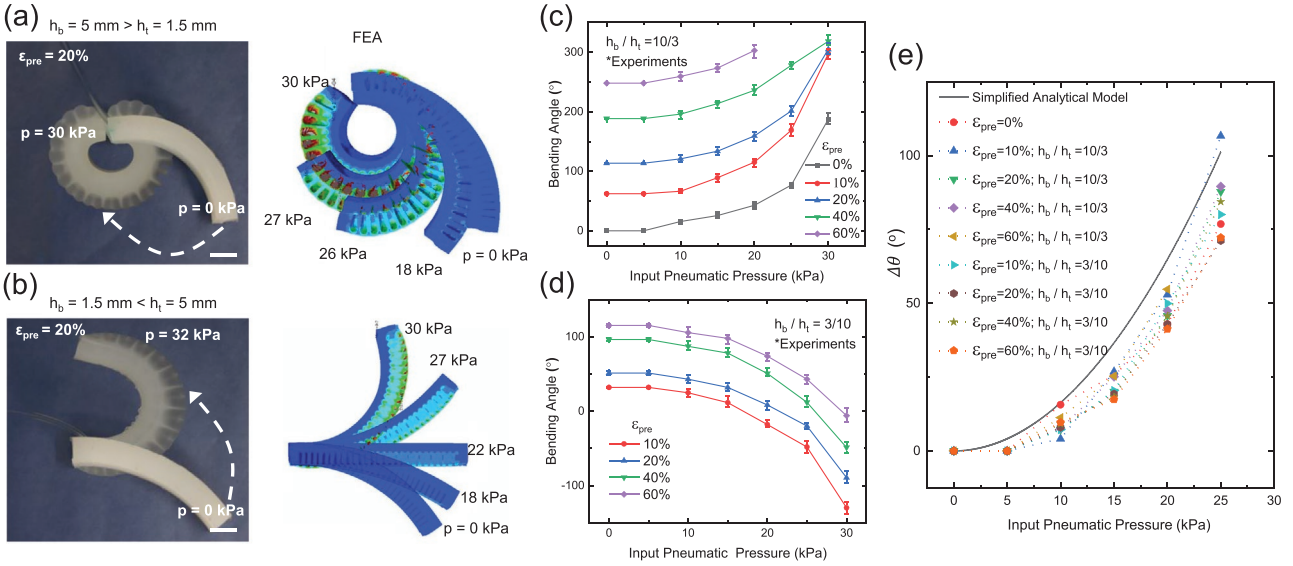


**Figure 3.** a,b) Comparison of actuated bending of pre-curved 2D soft bilayer actuator ($h_b$ = 5 mm and $h_t$ = 1.5 mm) and its counterparts ($h_b$ = 1.5 mm and $h_t$ = 5 mm) with prestrain $\varepsilon_{pre}$ = 20% under pneumatic pressure $p \approx$ 30 kPa. Scale bar: 10 mm. Corresponding FEA simulation results on the deformed shapes at different pressure are shown to the right. c,d) Measured actuated bending angle versus pneumatic pressure at different prestrain in experiments for actuators with $h_b$ = 5 mm and $h_t$ = 1.5 mm (c) and their counterparts with $h_b$ = 1.5 mm and $h_t$ = 5 mm (d), respectively. e) Comparison between the simplified analytical model and experiments on bending angle change versus pneumatic pressure for actuators with different thickness ratio and prestrain.

$\varepsilon_{pre}$, which exhibit a highly nonlinear correlation. For actuators with $h_b > h_t$, $\theta$ remains positive and increases monotonically with $p$ to close the actuators, where $\theta$ increases slightly with $p$ under lower actuation pressure ($0 < p < 20$ kPa), followed by a steep rise when $p$ is beyond 20 kPa. A similar trend is found in their counterparts with $h_b < h_t$, where $\theta$ decreases monotonically with $p$ from a positive to a negative value with the bending direction flipped. Corresponding FEA simulations (Figure S2, Supporting Information) on the actuated bending angles of both types of actuators under pneumatic pressure are consistent with the experiments. Moreover, when plotting different curves of $\theta$–$p$ to the bending angle change $\Delta\theta = |\theta - \theta_o|$ with respect to its original bending angle $\theta_o$ before actuation, all the curves of $\Delta\theta$–$p$ for actuators with different $\varepsilon_{pre}$ are close to each other and collapse onto similar nonlinear curves (Figure 3e). To better understand the nonlinear relationship between the input pressure $p$ and corresponding $\Delta\theta$ in the experiment, a simplified analytical model is developed based on the Euler–Bernoulli beam theory by assuming linear elastic materials response,[16] which gives (Supporting Information):

$$\Delta\theta = c_1 p^2 + c_2 p \tag{2}$$

where $c_1$ and $c_2$ are two constants determined by both the materials properties and geometry of the bending actuators. Figure 3e shows that the theoretical curve of Equation (2) captures the nonlinear monotonic increasing trend of $\Delta\theta$ with $p$, which is consistent with the experimental data. The observed discrepancy is due to both the assumed linear elastic materials model by neglecting the hyperelasticity in the elastomeric materials and simplified air channels by neglecting the complicated geometry of the zig-zag air channels in the simplified model.

### 2.2.3. Effect of Bilayer Thickness Ratio on Actuated Bending Behavior

To further explore the effect of different thickness ratios of $h_b/h_t$ on the distinct actuated bending behavior, we conduct a parametric FEA study on the deformation of the arched bending actuators by tuning the value of $h_b/h_t$ from below to above 1, where $\varepsilon_{pre}$ = 20% and pneumatic pressure $p$ = 40 kPa are kept the same. Specially, we choose three cases with their thickness ratio close to 1 for comparison, i.e., $h_b/h_t = 6/7$ (≈0.86) < 1, $h_b/h_t = 1$, and $h_b/h_t = 7/6$ (≈ 1.17) > 1.

**Figure 4** shows the bending angle change $\Delta\theta = |\theta_{p=30kPa} - \theta_o|$ at $p$ = 30 kPa for actuators with different $h_b/h_t$. For $h_b/h_t = 1$, i.e., the top and bottom layers have the same thickness, its bending angle barely changes ($\Delta\theta \approx 0^o$) under actuation due to the deformation symmetry with the same bending stiffness of the top and bottom layer. Figure 4ii shows that as $p$ increases, the arched actuator undergoes global inflation even at a higher pressure of 40 kPa without bending up or down further. However, when the deformation symmetry is broken by setting a slightly biased top and bottom layer thickness, the actuator starts to either unbend for $h_b/h_t = 6/7$ (Figure 4i) or bend further for $h_b/h_t = 7/6$ (Figure 4iii), showing a nonzero bending angle change of $\Delta\theta = 10^o$ and $\Delta\theta = 60^o$, respectively. Meanwhile, both actuators exhibit prominent longitudinal extension accompanied by bending. When $h_b/h_t$ is further away from 1 (e.g., $h_b/h_t = 3/10$ and 10/3), both actuators exhibit a large value of bending angle change over 150°. The results demonstrate that the thickness ratio of $h_b/h_t = 1$ defines a critical value to guide the distinct bending behavior under actuation. As actuation input increases, a pre-strained actuator with $h_b/h_t < 1$ prefers to unbend and flip to the opposite bending direction, while a pre-strained actuator with $h_b/h_t > 1$ tends to bend further with increased curvature.

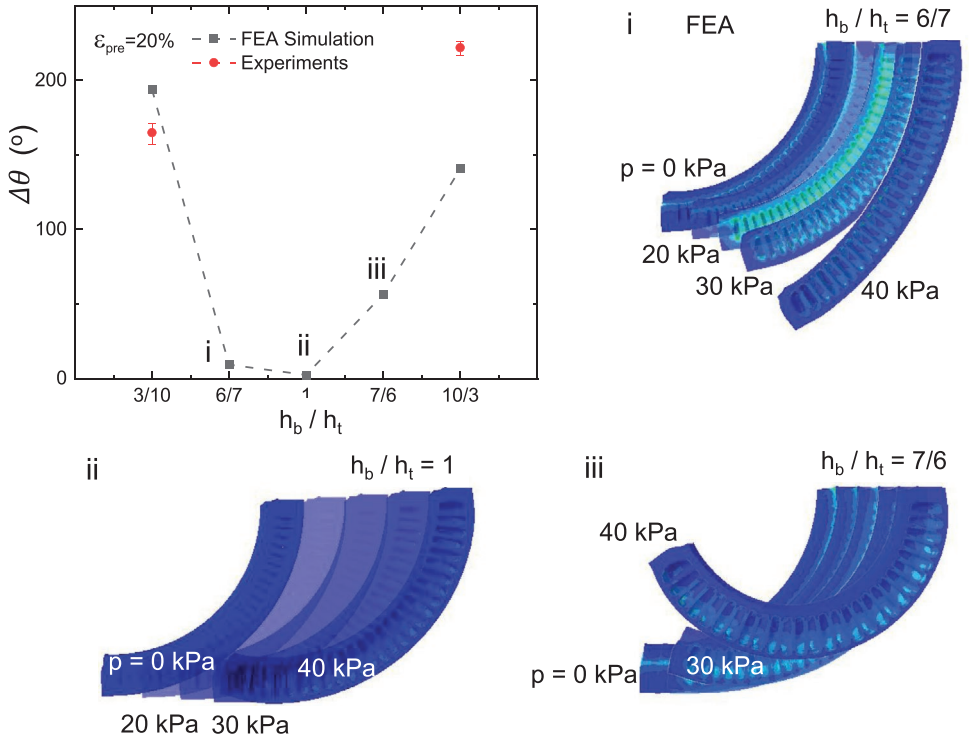


**Figure 4.** Bending angle change for actuators with different bilayer thickness ratios $h_b/h_t$ under $p = 30$ kPa. The corresponding FEA simulated deformed shapes under intermediate pressure values are shown in (i) for actuators with $h_b/h_t = 6/7$, in (ii) for actuators with $h_b/h_t = 1$, and in (iii) for actuators with $h_b/h_t = 7/6$.

### 2.3. 3D Pre-Curved Soft Doming Actuators

#### *2.3.1. Bifurcated Shape Change After Biaxial Prestrain Release*

Similar to the bistrip-based 2D bending actuators, a 3D doming actuator can be generated upon the release of equi-biaxially pre-strained circular plate (Figure 1b). **Figure 5**a,b shows the comparison between two cases of doming actuators with switched top stress-free layer ($h_t$ = 1.5 mm) and bottom pre-stretched layer thickness ($h_b$ = 3.5 mm) at different prestrains $\varepsilon_{pre}$, where the channel height $h_c$ and original diameter of the circular plate $D$ are kept the same with $h_c$ = 1 mm and $D$ = 60 mm. Both actuators exhibit similar shape transitions from a dome-like to warping shape with the increase of $\varepsilon_{pre}$, where isometric rotational symmetry in a dome is broken due to curvature induced buckling bifurcation. When $\varepsilon_{pre}$ is relatively small (e.g., $\varepsilon_{pre}$ = 10%, 20%), both actuators form a dome shape with uniform curvature as shown in Figure 5a (i-ii),b(i-ii). However, when $\varepsilon_{pre}$ is beyond a critical strain (≈30%), the dome shape becomes unstable and bifurcates to a warping shape (e.g., $\varepsilon_{pre}$ = 40%) as shown in Figure 5a (iii),b(iii), which is consistent with the corresponding FEA simulation results (right of Figure 5a,b). Correspondingly, the doming angle $\theta_d$ defined in the inset of Figure 5c increases monotonically with $\varepsilon_{pre}$. Figure 5c shows that the actuator with a thicker pre-stretched layer ($h_b$ = 3.5 mm > $h_t$ = 1.5 mm) exhibit both a larger doming angle and higher doming height than its counterpart ($h_b$ = 1.5 mm < $h_t$ = 3.5 mm), which are well reproduced by corresponding FEA simulations.

The bifurcation from a doming to warping shape can be explained from the curvature induced buckling instabilities of plates. It is known that flat plates of radius $R$ bifurcate at a critical doming angle of $\theta_{bifur}$ = (180° $D/\pi$) ($ah/R^2$) with $a = \sqrt{10+7\sqrt{2}}$,[17] where $D$ is the diameter of the circular plate. For the studied bilayer plate, $\theta_{bifur}$ is theoretically predicted to be $\theta_{bifur}$ = 102.2°. For actuators with small prestrain (e.g., $\varepsilon_{pre}$ = 10%, 20%), their doming angles are below $\theta_{bifur}$ (dashed line in Figure 5c). Thus, a rotationally symmetric dome shape is observed in both experiments and simulations, which is consistent with the theoretical prediction. However, as the prestrain further increases, their curvature and doming angle also increase. Theoretically, when the doming angle is beyond $\theta_{bifur}$, the bilayer cap cannot maintain a symmetric dome shape with higher strain energy and bifurcates to a warping shape to release the energy. This is consistent with the observed warping shapes of actuators with $\varepsilon_{pre}$ = 40% in both experiments and simulations, where their doming angles are much larger than $\theta_{bifur}$ (dashed line in Figure 5c).

#### *2.3.2. Tunable Monostable and Bistable Bending Behavior*

Upon pressurized actuation, **Figure 6**a,b shows that the two doming actuators exhibit distinct bending behavior. As the air pressure increases from 0 to 30 kPa, the doming actuator with a thicker pre-stretched bottom layer ($h_b$ = 3.5 mm > $h_t$ = 1.5 mm) continues to bend downward due to the expansion of air channel in the top layer (Figure 6a). Figure 6c shows that

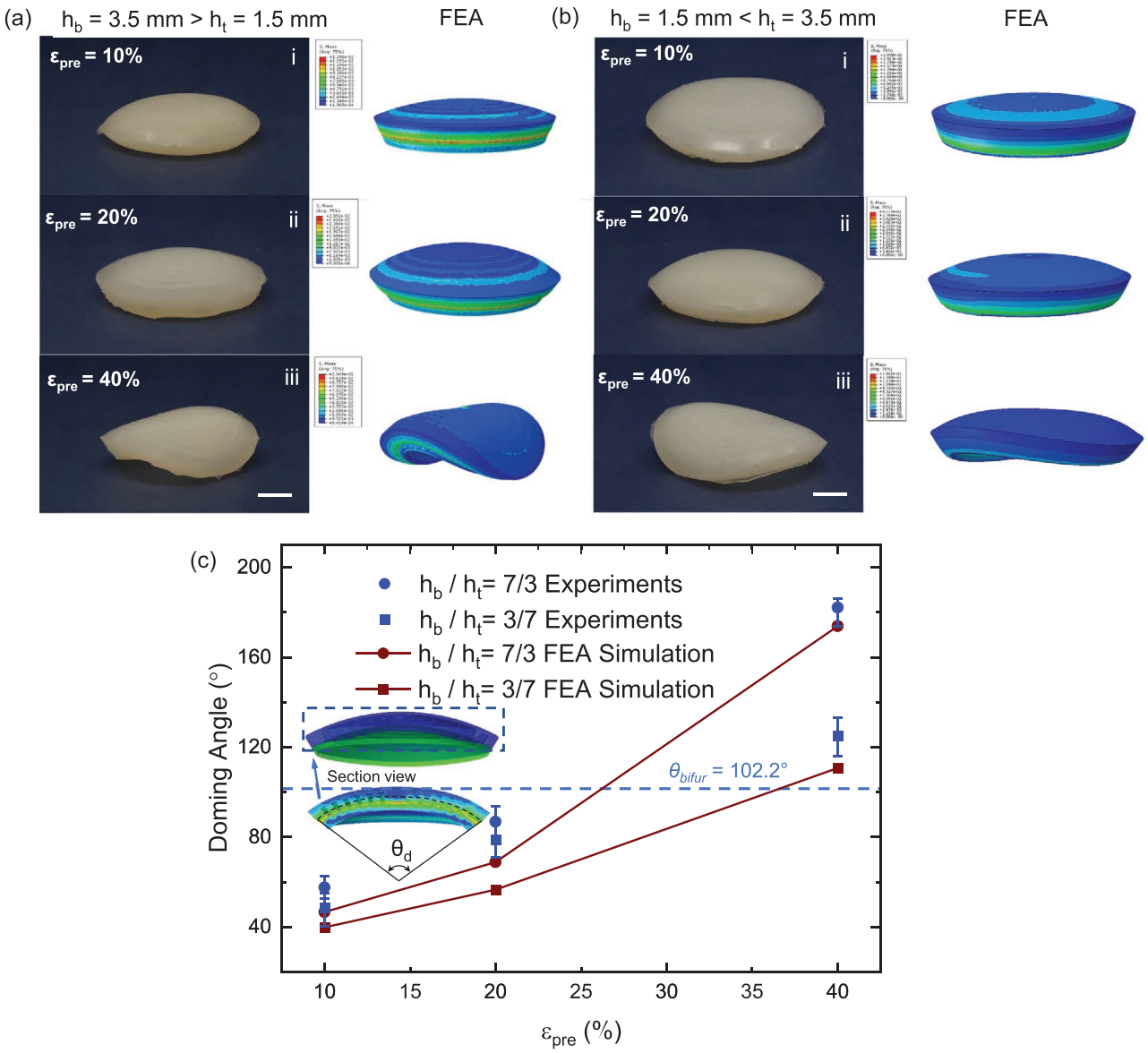


**Figure 5.** a,b) Comparison of pre-curved 3D soft doming actuators with $h_b = 3.5$ mm and $h_t = 1.5$ mm (a) and their counterparts with $h_b = 1.5$ mm and $h_t = 3.5$ mm (b) after the release of different prestrains $\varepsilon_{pre}$. Scale bar: 10 mm. Corresponding FEA simulation results on the deformed shapes are shown to the right. c) Comparison of doming angle $\theta_d$ versus prestrain $\varepsilon_{pre}$ between experiments and FEA for 3D doming actuators and their counterparts with different bilayer thickness ratio $h_t/h_b$. Dashed line represents the theoretically predicted bifurcation doming angle $\theta_{bifur}$.

the doming angle $\theta_d$ increases monotonically with the pressure for actuators with different $\varepsilon_{pre}$, which is consistent with the corresponding FEA simulation (Figure S3a, Supporting Information; Figure 3c). When the pressure is beyond 25 kPa, localized distortion occurs on the top. On contrary, for its counterpart with switched bilayer thickness ($h_b$ = 1.5 mm < $h_t$ = 3.5 mm), as the pressure increases, it transits from an initial warping shape to a symmetric doming shape, then bends upward and flips its doming direction with further increase of pressure. Consequently, $\theta_d$ decreases monotonically and becomes negative when it bends upward (Figure 6d). Similar trend of decreasing $\theta_d$ from positive to negative value with pressure is captured by the FEA simulations (Figure S3b,d, Supporting Information).

Interestingly, unlike the continuous decrease of $\theta_d$ with pressure, the actuator with a relatively large prestrain (e.g., $\varepsilon_{pre}$ = 40%) exhibits a sharp drop of $\theta_d$ from 75° to –125° as the pressure is increased beyond a threshold value of 15 kPa (Figure 6d). It corresponds to a snap-through bistability as illustrated in the schematic energy profile (Figure 6e). The planar configuration (unbent) represents an unstable state with the local maximum strain energy (State II in Figure 6e), which is equal to the stretching energy in the pre-stretched layer, and two configurations, doming-up with positive doming angle (State I in Figure 6e) and doming-down with negative doming angle (State III in Figure 6e), represent two stable states with local minimum strain energy after pre-stretching energy release. We further confirm the snap-through bistability by monitoring the

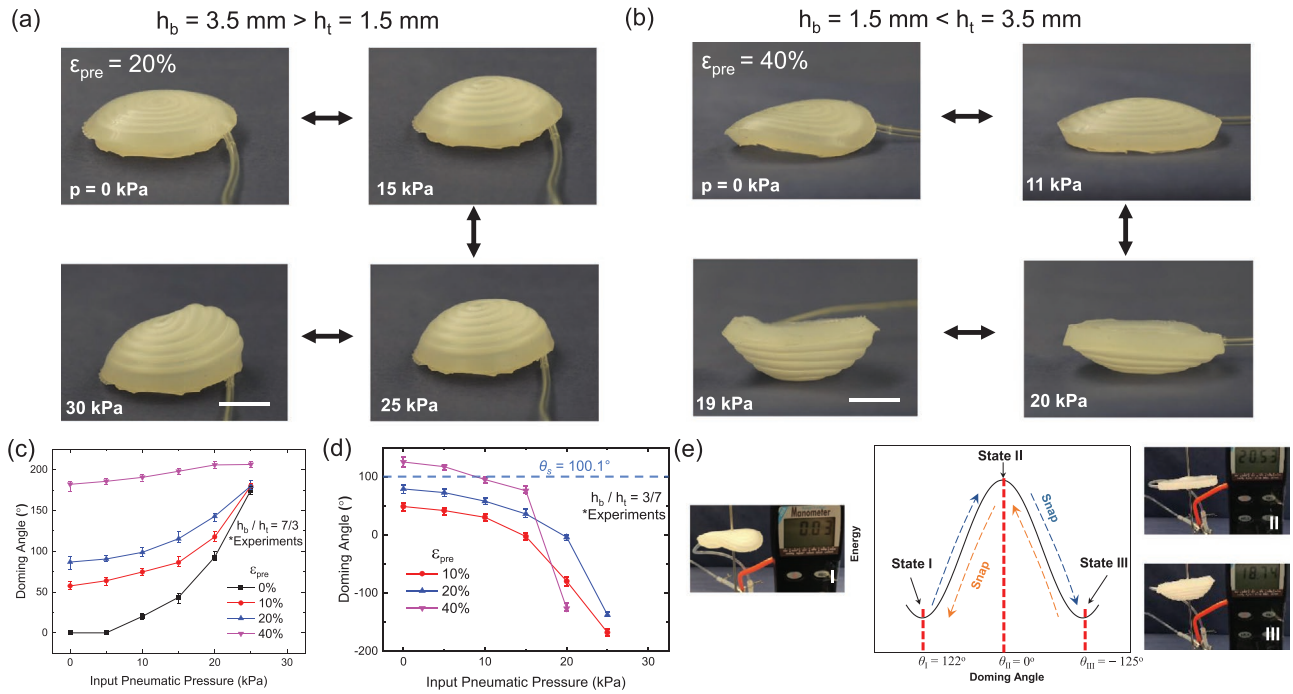


**Figure 6.** a,b) Comparison of actuated bending of pre-curved 3D soft doming actuator ($h_b$ = 3.5 mm and $h_t$ = 1.5 mm) and its counterparts ($h_b$ = 1.5 mm and $h_t$ = 3.5 mm) with respective prestrain $\varepsilon_{pre}$ = 20% and $\varepsilon_{pre}$ = 40% under pneumatic pressure. Scale bar: 20 mm. c,d) Measured actuated doming angle versus pneumatic pressure at different prestrain in experiments for actuators with $h_b$ = 3.5 mm and $h_t$ = 1.5 mm (c) and their counterparts with $h_b$ = 1.5 mm and $h_t$ = 3.5 mm (d), respectively. Dashed line in (d) represents the theoretically predicted doming angle $\theta_s$ for the occurrence of snap-through bistability. e) Schematic energy profile as a function of doming angle for the bistable pre-curved doming actuator with $\varepsilon_{pre}$ = 40%. The snapshots show the shape changes under actuation with recorded pressure change at representative states of I, II, and III.

pressure change using a manometer (Omega Engineering, Inc) under actuation (slow motion in Video S1, Supporting Information). To capture the transient snap-through process, the doming actuators are quasi-statically pumped and pressurized with a slow airflow rate of 0.5 L min$^{-1}$. We observe that when the actuator bypasses the unstable state, it quickly snaps to the flipped state and the response time for the transient snapping-through process takes about 0.5 ± 0.1 s. Meanwhile, there is a slight pressure drop from 20.5 kPa (State II) to 18.7 kPa (State III) due to the release of strain energy during the snapping-through process (Video S2, Supporting Information). In contrast, no pressure drop is observed for other flipping soft actuators with small prestrain when bypassing the straight configuration.

Similarly, the observed actuated snap-through bistability can be understood throu≠gh the curvature-induced buckling of shells.[18] We consider the doming actuators as a family of circular thin shells with fixed thickness $h$ and $R$ but with different doming angle $\theta_d$. The pressurized process is simplified as a pure curvature changing without any global inflation. The actuated deformation can be decomposed into bulk deformation within the center area and bending deformation in the boundary. The competition between the center and boundary layer determines the instability. Since the width of the boundary scales with $\sqrt{Rh}$, actuators with larger bending radius $R$ (i.e., smaller prestrain) possess a wider boundary region compared to ones with smaller radius (i.e., larger prestrain). Thus, for shells with larger $R$, bending deformation of the wider boundary dominates the deformation of the shell and reverses its deformation smoothly as actuation increases. There exists a critical dimensionless critical doming angle $\overline{\theta}_s$ = 2.09 so that shells with $\overline{\theta}_d < \overline{\theta}_s$ do not snap,[18] where $\overline{\theta}_d = \theta_d / 2\sqrt{h/R}$. For the studied doming actuator, we have the theoretically predicted critical doming angle of $\theta_s$ = 100.1° for snap-through bistability (Supporting Information). For actuators with small prestrain, e.g., $\varepsilon_{pre}$ = 10% and 20%, we have $\theta_d < \theta_s$ (Figure 6d), thus, smooth flipping without snap-through is observed. However, for actuator with large prestrain, e.g., $\varepsilon_{pre}$ = 40%, $\theta_d$ is larger than $\theta_s$ and the snap-through bistability occurs as observed in the experiment.

### 2.4. Multifunctional Robotic Applications

#### *2.4.1. Energy-Efficient Soft Gripper*

By utilizing the flipping feature of 2D arched bending actuators with a thinner bottom pre-stretched layer ($h_b < h_t$) in Figure 3b, we design an energy-efficient soft gripper that is composed of four identical prestrained 2D arched actuators with $h_b$ = 1.5 mm and $h_t = h_c$ = 5 mm as "fingers" (**Figure 7**a). A prestrain of $\varepsilon_{pre}$ = 100% is set in terms of Equation (1) to generate a bending angle of 180° for each actuator after pre-strain release, thus, the gripper forms an initial closed "finger" configuration before actuation (Figure 7b (i)) for potentially holding an object through prestress without actuation inputs.

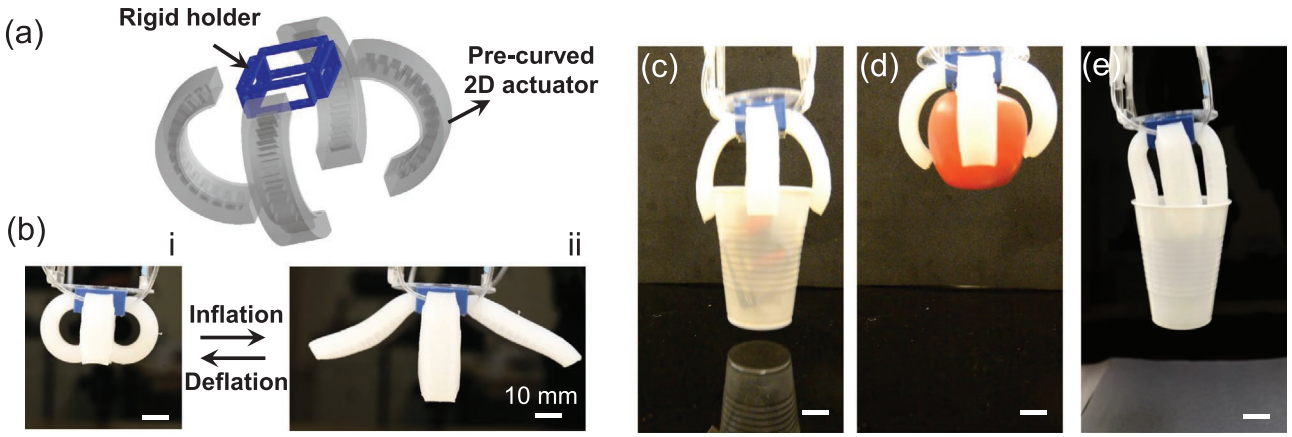


**Figure 7.** a) Schematic of pre-curved soft gripper composed of four identical 2D bilayer bending actuators with a thinner pre-stretched layer. b) Initial "fingers" closed state without pressurization for holding certain weight (i) and pressurized for flipping bending direction to open the "fingers" for potential grasping and releasing (ii). c–e) demonstration of grasping a plastic cup filled with a weight of objects of 240 g (c), an apple (d), and a plastic cup from inside (e). Scale bar: 10 mm.

We used two air pumps to control the inflation and deflation of respective front/back and left/right "fingers" separately, which provides us more independent control on the bending deformation of each "finger." Upon pneumatic pressurization, the bending actuators flip and bend outward to open the gripper for grasping objects (Figure 7b (ii)). We demonstrate in Figure 7c–e and Video S3, Supporting Information, that the soft gripper can grasp and lift a plastic cup filled with a weight of up to 240 g (Figure 7c), which is three times the self-weight of the soft gripper, as well as grasp an apple with a regular curved shape (Figure 7d). Furthermore, we demonstrate that it can also grasp the plastic cup from inside by constraining the bending deformation of actuators inside the cup for holding through inner wall friction (Figure 7e). The slight difference in actuated bending angles of front/back "fingers" and front/back "fingers" is due to the different flow rates in the two air pumps. Note that the pre-bent "finger" shapes of our proposed grippers are contrary to the conventional design of soft grippers with initial straight tubular "finger"[19] before actuation. Upon actuation input, conventional grippers bend their "fingers" and hold the object for transporting to target locations, where the grippers need to be actuated persistently during transportation and cost energy. By contrast, our proposed pre-curved soft gripper only consumes certain energy to open the initially closed "fingers" to grasp the targeted objects. During transportation, it can hold the object by utilizing the prestress at resting states without consuming energy (under non-actuated states) or reducing the energy consumption with less actuation input.

### 2.4.2. Fast Crawling Soft Robot

Inspired by the fast jumping locomotion of fruit-fly larva through curling its soft body to store and release energy,[20] we demonstrated a fast crawling soft robot based on monotonic bending of 2D pre-curved bistrip actuators (**Figure 8**a). To break the symmetric deformation and store energy for fast propelling during locomotion, we added an extra weight in the head of the crawler with a steel rod (Figure 8a (i)), as well as introduced a height gradient to the embedded air channels, where the channel height increases linearly from the head to the rear with lower end $h_{cl}$ = 3.5 mm and higher end $h_{ch}$ = 4.5 mm. Consequently, the gradient air channels lead to a compromised thickness gradient in the stress-free top layer to achieve a uniform total layer thickness of 7 mm on top of the pre-stretched layer. To ensure a monotonic bending as discussed before, the thickest layer thickness in the stress-free top layer ($h_{th}$) is set to be thinner than the pre-stretched layer on the bottom, i.e., $h_{th}$ = 2.5 mm < $h_b$ = 3.5 mm. The pre-stretched layer is set to be wider than the top layer to help keep the balance during locomotion.

Figure 8b shows the locomotion mechanism for the soft crawler with $\varepsilon_{pre}$ = 20% with snapshots from its slow-motion video (Video S4, Supporting Information) on a sandpaper (800 girds) with a relatively high roughness. After the prestrain release, the arched soft crawler exhibits a nearly symmetric bent configuration with line contact in both the front and rear (Figure 8b (i)). Upon inflation, its rear undergoes a larger bending rotation than the front due to its higher channel height induced larger expansion. Thus, the soft body deforms into an asymmetric arch shape (Figure 8b (ii)), where the body length is shortened after bending and the original line contact transits to surface contact. As the pneumatic pressure increases, its rear further curls like a spring to store more strain energy with the help of its heavier head induced larger static friction force in the front. Upon deflation by decreasing air pressure, the elastic strain energy stored in the spring-like rear is quickly released and the curled soft body recovers to its original shape. The energy release generates a large instantaneous thrust force to lift off the head from the ground to extend its stride length (Figure 8b (iii)), thus the soft crawler locomotes forward during a cycle of pneumatic pressurization and depressurization (Figure 8b (iv)). During locomotion, since a larger static friction force can help holding the rear part to facilitate the energy storage by curling the soft body, thus, we expect that a relatively rough surface will enhance the locomotion distance in one cycle to further speed up the crawler.

Next, we explore the effect of the prestrain on the locomotion speed of the soft crawler on the same flat sandpaper surface

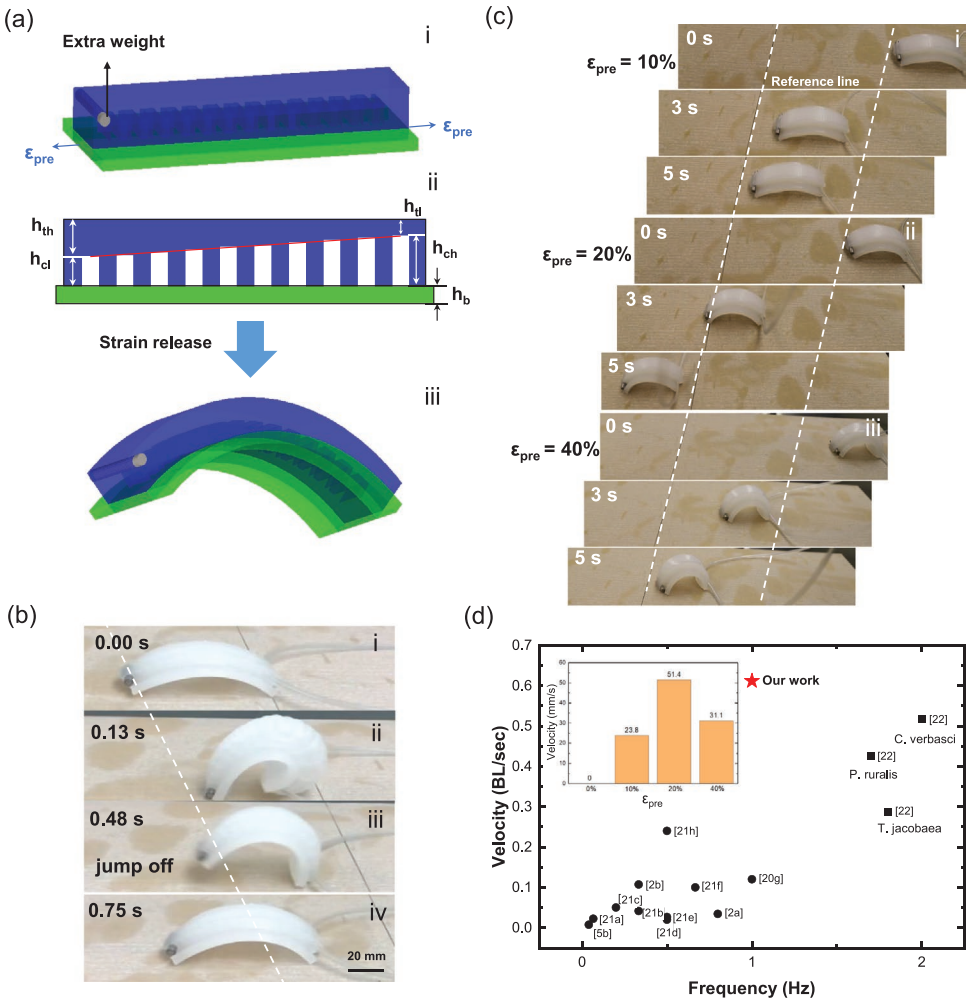


**Figure 8.** a) Schematic of design of fast pre-curved soft crawler based on pre-stressed bilayer actuator with gradient channel height and added extra weight in the front. b) Slow motion shows the crawling process by curling its rear to store energy and lift off its head through energy release. c) Comparison of the average locomotion speed between pre-curved crawlers with different prestrains $\varepsilon_{pre}$ = 10%, 20%, and 40% under the same pressure of 30 kPa and actuation frequency of 1 Hz. d) Comparison of the average locomotion speed between our crawler and other reports of soft crawlers (solid circular symbols) and different species of fast locomoting caterpillars (solid square symbols) in terms of actuation frequency. Inset shows the velocity of our crawlers at different prestrains.

(800 grids). A group of 4 crawlers are compared with identical gradient channel size and layer thickness but with different pre-stretched strain of $\varepsilon_{pre}$ = 0% (no pre-stretch), $\varepsilon_{pre}$ = 10%, $\varepsilon_{pre}$ = 20%, and $\varepsilon_{pre}$ = 40%, respectively, as shown in Figure 8c and Video S5, Supporting Information. The actuation pressure of 30 kPa and actuation frequency of 1 Hz are kept the same. For the crawler with $\varepsilon_{pre}$ = 0%, it takes an initial straight body shape. Upon actuation, it can barely move due to the large friction and the gravity to resist bending up. Further increase of pressure induces the global inflation of its soft body. In contrast, all pre-curved crawlers are able to move under actuation as shown in Figure 8c. Among the three crawlers, the crawler with $\varepsilon_{pre}$ = 20% achieves the highest average locomotion speed of 51.4 mm $s^{-1}$ or 0.65 body length $s^{-1}$ (BL/s), which is 2.2 times the speed of the crawler with $\varepsilon_{pre}$ = 10% and 1.6 times the speed of the crawler with $\varepsilon_{pre}$ = 40% (inset of Figure 8d).

The locomotion speed is determined by the initial pre-curved shapes upon release of different prestrain and the actuated shape change. The curvature of the arched crawler increases with $\varepsilon_{pre}$, i.e., as $\varepsilon_{pre}$ increase, its body length decreases while its height increases. Thus, under the same pneumatic pressurization, the crawler with smaller curvature can store more strain energy through curling its rear body, which produces a higher propelling force after energy release for a potential faster speed. However, its higher force is compromised by its relatively shorter body length, which consequently extends a smaller stride length after energy release to lower its locomotion speed. Such a compromise between larger energy release and shorter body length explains the highest speed observed in the crawler with an intermediate strain of $\varepsilon_{pre}$ = 20%.

We further compared the fast speed of the soft arched crawler with the locomotion speed of a few representative soft robots[2a,b,5b,21] and different species of fast locomoting caterpillars[22] by categorizing them in the chart of body length speed versus actuation frequency in Figure 8d. These soft crawlers show a slow average speed in the range of 0.02–0.24 BL $s^{-1}$.

Despite different actuation mechanisms and soft materials employed in previous reported soft crawlers, including pneumatic pressurization, light, electrical and magnetic field, and humidity, our pre-strained crawler demonstrated an outperforming higher average speed of 0. 65 BL $s^{-1}$, which is 2.7 times faster than the ratcheted actuator-based superior-velocity soft Hygrobot actuated by environmental humidity.[21h] Such a speed is even faster than the fastest locomoting caterpillar *C. verbasci* but with only half of its frequency of 1 Hz.

### 2.4.3. Fast Swimming Bistable Jellyfish-Like Soft Robot

Inspired by the doming configuration during the underwater swimming of jellyfish, we designed a fast swimming bistable soft robot by utilizing the snap-through bistability of 3D doming bilayer actuator. **Figure 9**a shows the schematic design of the soft swimmer by attaching swimming paddles to the bistable 3D doming actuator with $\varepsilon_{pre}$ = 40% in Figure 5b to amplify the thrust force. The layer thickness is set to be the same as that in Figure 5b with a thinner pre-stretched layer ($h_b$ = 1.5 mm < $h_t$ = 3.5 mm). After the pre-strain release, the bilayer plate bends rightward, forming a shallow dome before actuation (Figure 9b). Upon pressurization, it snaps through to the left side, forming a deep dome shape to push the enclosed water and propel itself forward. Under pneumatic pressure of 30 kPa and frequency of 0.67 Hz, the bistable soft robot can achieve an average linear speed of 53. 3 mm $s^{-1}$ (Figure 9c), which is 1.4 times faster than its stable counterpart without prestrain (i.e., the initial configuration is a planar bilayer plate; Figure 9d; Video S6, Supporting Information), demonstrating the benefit of bistability in enhancing the swimming speed.

We further compared the speed of the bistable swimmer with different species of natural jellyfish[23] and other reported jellyfish-inspired soft robotic swimmers.[2d,24] It shows that our bistable soft swimmer is twice faster than the natural jellyfish *Mitrocoma cellylaria* with similar frequency.[23] For soft robotic swimmers, their dome-like structures are inherently designed to be stable and their speed is approximately proportional to the actuation frequency.[2d,24] At a frequency of 5.2 Hz, previous studies report a fast speed of 53 mm $s^{-1}$ in the biomimetic robotic jellyfish actuated by high-energy-density shape memory alloy composite actuators.[24d] In contrast, the proposed bistable

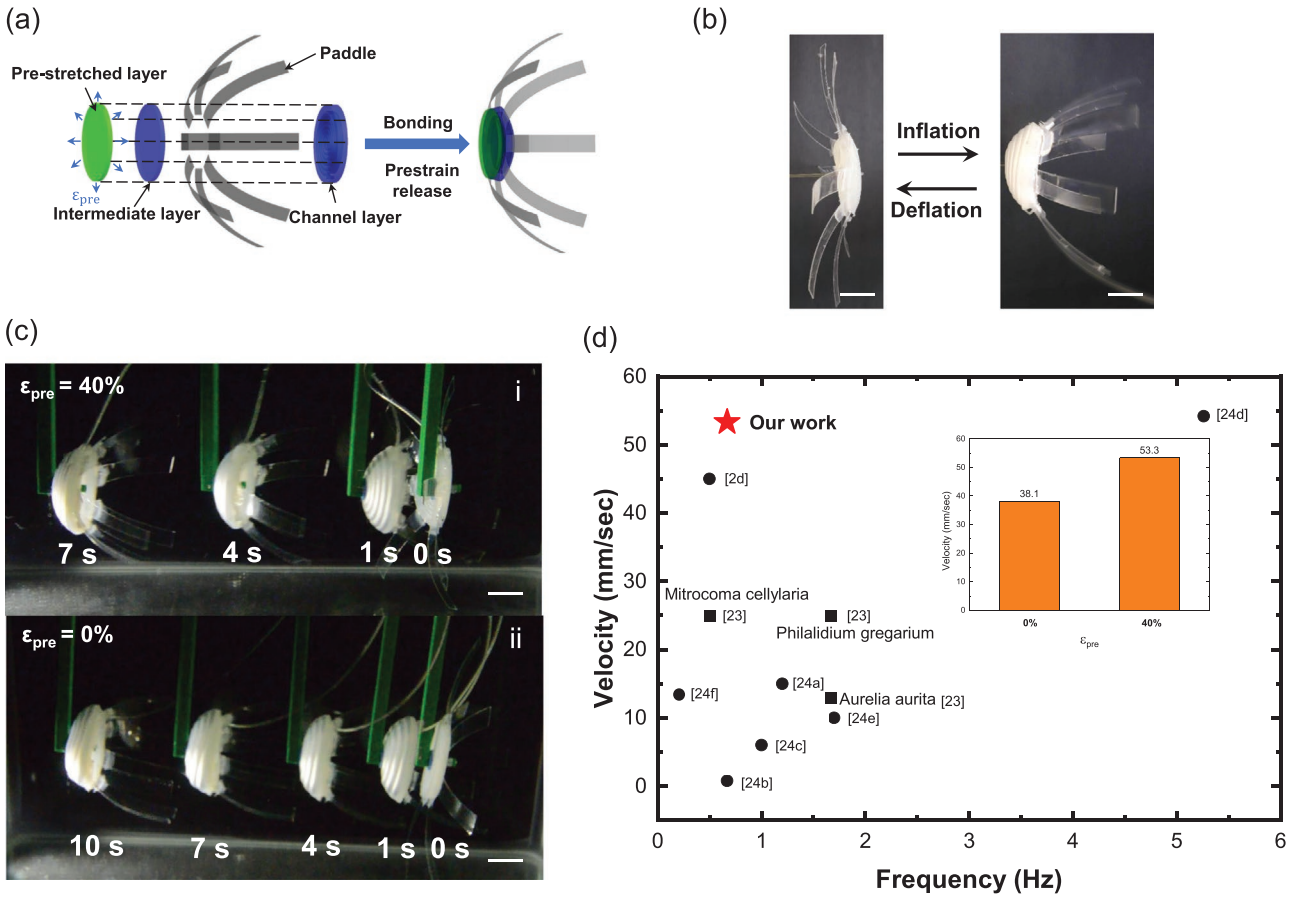


**Figure 9.** a) Schematic of design of fast jelly-fish-like soft swimmer based on bistable pre-strained bilayer doming actuators. b) Bistable switch of soft swimmer under pressurization by flipping its doming direction. c) Comparison of locomotion between bistable soft swimmer and its stable counterpart without prestrain. d) Comparison of the average swimming velocity between our bistable swimmer and natural jelly fish (solid square symbols) and other reports of jelly-fish-like soft swimmer in terms of frequency (solid circular symbols). Inset shows the average velocity of our bistable swimmer and its stable counterpart without prestrain. (scale bar in all figures: 20 mm)

swimmer can achieve a comparable speed at a much lower actuation frequency of 0.67 Hz despite its constituent lower energy density elastomeric materials.

## 3. Conclusion

In summary, we present a simple strategy of leveraging mechanical pre-stretch relaxation in generating pre-curved 2D bilayer bending and 3D doming actuators for designing multitask high-performance soft robots. By switching the biased thickness between the pre-stretched layer and strain-limiting layer, the actuated bending direction in both 2D and 3D actuators can be flipped and their monostability and bistability can be tuned by manipulating the pre-stretched strain. By utilizing the strain energy storage/release through pre-stretching, we demonstrate the applications of both monostable/bistable 2D and 3D actuators to a variety of high-performance soft robotics, including energy-saving soft gripper, fast-speed soft crawler, and fast jelly-fish-like soft swimmer. Despite the demonstration of pneumatic actuation in conventional elastomeric materials, we envision that the strategy of harnessing pre-stretch relaxation for monostable and bistable pre-curved soft bending actuators in 2D and 3D can be applied to other widely used soft materials in soft actuators and soft robotics to further boost their outperforming robotic multifunctionality, including shape memory polymers or alloys, electroactive polymers, and stimuli-responsive materials in response to different actuation inputs such as heat, electricity, light, and magnetic field.

## 4. Experimental Section

*Actuator Fabrication*: All pneumatic bilayer actuators were fabricated following the typical manufacturing strategy for fluid-driven soft actuators through molding and demolding approaches. Ecoflex 00–50 (Smooth-on Inc) was used as the elastomeric materials for the homogeneous pneumatic bilayer actuators. The bilayer including the layer for pre-stretching and the pneumatic channeled layer was fabricated by directly peeling off from 3D printed molds by Ultimaker 3 Extended after curing in an oven at 70 °C for 1 h. The cured Ecoflex layer was manually pre-stretched and clamps were used to fix the pre-stretched state to a glass slide. Then the pre-streched layer was glued with the stress-free pneumatic channel layer by uncured Ecoflex 00–50 and cured them at 70 °C for 1 h. Finally, the pre-strain was released to form a pre-curved configuration at room temperature.

*Soft Crawling Robot Fabrication*: Based on the fabrication process described above, a gradient height was introduced to the air channel in the 2D bending actuator with $\Delta h = 1$ mm along the actuator. The extra weight was added to the head of the soft crawler by inserting a steel cylindrical rod with a diameter of 4.8 mm and length of 24.7 mm. The width of the pre-stretched layer was set to 40 mm, which was twice wider than the air channel layer.

*Soft Gripper Fabrication*: The soft gripper consisted of four flipping pre-curved 2D bending actuators with $\varepsilon_{pre} = 40\%$ and a rigid frame. The central rigid frame made of PLA was 3D printed by Ultimaker 3 Extended.

*Soft Swimmer Fabrication*: As illustrated in Figure 9a, the outermost cover layer denoted as green color was first pre-stretched to a certain strain and bonded to a stress-free channel layer highlighted with blue color. Eight curled swimming paddles made of plastic thin strips were embedded into the interface between the cover layer and pneumatic channel layer along the edge of the circular shape. The swimming paddles were made of shrink paper with dimensions of 80 mm × 15 mm × 0.29 mm cut by a laser cutter. The straight stripes were curved with a bending angle of 41.67° and placed at 100 °C for 1 h for thermosetting.

*Actuated Bending Angle Measurement*: The actuator was connected to a syringe and a manometer (Omega Engineering, Inc) with the rubbery tube. With the pumping by syringe, the bending angle and the pressure were both captured by the camera simultaneously.

*FEA Simulation*: To investigate the prestrain releasing and pneumatic actuation processes of all bilayer actuators, 3D models were built by Solidworks software and the commercial FEA software Abaqus/CAE was used for analysis, employing the Abaqus/Standard solver. The geometry of all actuators was imported into Abaqus CAE as an stl file and mesh with solid quadratic tetrahedral elements (C3D10H). A mesh refinement study was applied to verify the accuracy of the mesh. The elastomer (Ecoflex-0050) was modeled as a hyper-elastic isotropic Yeoh model whose strain energy density is given by

$$U = \sum_{i=1}^{N} C_{i0}(\bar{I}_1 - 3)^i + \sum_{i=1}^{N} \frac{1}{D_i}(J-1)^{2i} \tag{3}$$

where $\bar{I}_1 = tr[dev(\mathbf{FF})^T]$, $J = \det(\mathbf{F})$, and $\mathbf{F}$ is the deformation gradient, and $C_{i0}$ and $D_i$ are the material parameters. In the model, $N = 3$, $C_{10} = 0.019$, $C_{20} = 0.0009$, $C_{30} = -4.75 \times 10^{-6}$, $D_1 = D_2 = D_3 = 0$. The prestretched layers were modeled as the same hyper-elastic Yeoh model with different thermal expansion coefficients to simulate the prestrain releasing process. Static simulations were performed by applying pressure on the internal surfaces of the cavities.

## Supporting Information

Supporting Information is available from the Wiley Online Library or from the author.

## Acknowledgements

J.Y. acknowledges the funding support from NSF CMMI-2010717 and CAREER-2005374.

## Conflict of Interest

The authors declare no conflict of interest.

## Keywords

bistability, locomotion, soft actuators, soft robotics, swimming

Received: April 18, 2020
Revised: May 26, 2020
Published online:

[1] a) D. Rus, M. T. Tolley, *Nature* **2015**, *521*, 467; b) C. Majidi, *Soft Robot.* **2014**, *15*; c) H. Lu, M. Zhang, Y. Yang, Q. Huang, T. Fukuda, Z. Wang, Y. Shen, N Comm. **2018**, *9*, 3944.

[2] a) R. F. Shepherd, F. Ilievski, W. Choi, S. A. Morin, A. A. Stokes, A. D. Mazzeo, X. Chen, M. Wang, G. M. Whitesides, *Proc. Natl. Acad. Sci. U. S. A.* **2011**, *108*, 20400; b) M. T. Tolley, R. F. Shepherd, B. Mosadegh, K. C. Galloway, M. Wehner, M. Karpelson, R. J. Wood, G. M. Whitdesides, *Soft Rob.* **2014**, *1*, 213; c) S. Taccola, F. Greco, E. Sinibaldi, A. Mondini, B. Mazzolai, V. Mattoli, *Adv. Mater.* **2015**,

 

*27*, 1668; d) W. Jiang, D. Niu, H. Liu, C. Wang, T. Zhao, L. Yin, Y. Shi, B. Chen, Y. Ding, B. Lu, *Adv. Funct. Mater.* **2014**, *24*, 7598.

[3] a) W. Hu, G. Z. Lum, M. Mastrangeli, M. Sitti, *Nature* **2018**, *554*, 81; b) H. Li, G. Go, S. Y. Ko, J.-O. Park, S. Park, *Smart Mater. Struct.* **2016**, *25*, 027001; c) A. A. Solovev, S. Sanchez, M. Pumera, Y. F. Mei, O. G. Schmidt, *Adv. Funct. Mater.* **2010**, *20*, 2430; d) H. Lu, Y. Hong, Y. Yang, Z. Yang, Y. Shen, *Adv. Sci.* **2020**, 2000069.

[4] a) N. Kellaris, V. Gopaluni Venkata, G. M. Smith, S. K. Mitchell, C. Keplinger, *Sci. Rob.* **2018**, *3*, eaar3276; b) E. Acome, S. K. Mitchell, T. G. Morrissey, M. B. Emmett, C. Benjamin, M. King, M. Radakovitz, C. Keplinger, *Science* **2018**, *359*, 61; c) B. Tondu, S. Ippolito, J. Guiochet, A. Daidie, *Int. J. Robotics Research* **2005**, *24*, 257.

[5] a) H.-T. Lin, G. G. Leisk, B. Trimmer, *Bioinspir. Biomim.* **2011**, *6*, 026007; b) M. Rogóż, H. Zeng, C. Xuan, D. S. Wiersma, P. Wasylczyk, *Adv. Opt. Mater.* **2016**, *4*, 1689; c) Y. Tang, Q. Zhang, G. Lin, J. Yin, *Soft Rob.* **2018**, *5*, 592; d) C. Laschi, M. Cianchetti, B. Mazzolai, L. Margheri, M. Follador, P. Dario, *Adv. Robotics* **2012**, *26*, 709; e) M. Calisti, A. Arienti, F. Renda, G. Levy, B. Hochner, B. Mazzolai, P. Dario, C. Laschi, 2012 IEEE International Conference on Robotics and Automation **2012**, 4950.

[6] a) P. Polygerinos, Z. Wang, K. C. Galloway, R. J. Wood, C. J. Walsh, *Robot. Auton. Syst.* **2015**, *73*, 135; b) Y.-L. Park, B.-R. Chen, N. O. Pérez-Arancibia, D. Young, L. Stirling, R. J. Wood, E. C. Goldfield, R. Nagpal, *Bioinspir. Biomim.* **2014**, *9*, 016007.

[7] T. Chen, O. R. Bilal, K. Shea, C. Daraio, *Proc. Natl. Acd. Sci. U. S. A.* **2018**, *115*, 5698.

[8] P. Rothemund, A. Ainla, L. Belding, D. J. Preston, S. Kurihara, Z. Suo, G. M. Whitesides, *Sci. Rob.* **2018**, *3*, eaar7986.

[9] J. T. B. Overvelde, T. Kloek, J. J. A. D'haen, K. Bertoldi, *Proc. Natl. Acad. Sci. U. S. A.* **2015**, *112*, 10863.

[10] Y. Tang, Y. Chi, J. Sun, T.-H. Huang, O. H. Maghsoudi, A. Spence, J. Zhao, H. Su, J. Yin, *Sci. Adv.* **2020**, *6*, eaaz6912.

[11] J. A. Rogers, T. Someya, Y. Huang, *Science* **2010**, *327*, 1603.

[12] a) S. Xu, Z. Yan, K.-I. Jang, W. Huang, H. Fu, J. Kim, Z. Wei, M. Flavin, J. McCracken, R. Wang, A. Badea, Y. Liu, D. Xiao, G. Zhou, J. Lee, H. U. Chung, H. Cheng, W. Ren, A. Banks, X. Li, U. Paik, R. G. Nuzzo, Y. Huang, Y. Zhang, J. A. Rogers, *Science* **2015**, *347*, 154; b) Y. Zhang, F. Zhang, Z. Yan, Q. Ma, X. Li, Y. Huang, J. A. Rogers, *Nat. Rev. Mater.* **2017**, *2*, 17019.

[13] B. J. Cafferty, V. E. Campbell, P. Rothemund, D. J. Preston, A. Ainla, N. Fulleringer, A. C. Diaz, A. E. Fuentes, D. Sameoto, J. A. Lewis, G. M. Whitesides, *Adv. Mater. Technol.* **2019**, *4*, 1800299.

[14] A. Pal, D. Goswami, R. V. Martinez, *Adv. Funct. Mater.* **2020**, *30*, 1906603.

[15] S. Timoshenko, *J. Opt. Soc. Am.* **1925**, *11*, 233.

[16] G. Alici, T. Canty, R. Mutlu, W. Hu, V. Sencadas, *Soft Rob.* **2018**, *5*, 24.

[17] M. Pezzulla, G. P. Smith, P. Nardinocchi, D. P. Holmes, *Soft Matter* **2016**, *12*, 4435.

[18] M. Pezzulla, N. Stoop, M. P. Steranka, A. J. Bade, D. P. Holmes, *Phys. Rev. Lett.* **2018**, *120*, 048002.

[19] B. Mosadegh, P. Polygerinos, C. Keplinger, S. Wennstedt, R. F. Shepherd, U. Gupta, J. Shim, K. Bertoldi, C. J. Walsh, G. M. Whitesides, *Adv. Funct. Mater.* **2014**, *24*, 2163.

[20] K. Oliver, A. Seddon, R. S. Trask, *J. Mater. Sci.* **2016**, *51*, 10663.

[21] a) W. Wang, J.-Y. Lee, H. Rodrigue, S.-H. Song, W.-S. Chu, S.-H. Ahn, *Bioinspir. Biomim.* **2014**, *9*, 046006; b) E. B. Joyee, Y. Pan, *Soft Rob.* **2019**, *6*, 333; c) M. A. Robertson, J. Paik, *Sci. Rob.* **2017**, *2*, eaan6357; d) J. Cao, L. Qin, J. Liu, Q. Ren, C. C. Foo, H. Wang, H. P. Lee, J. Zhu, *Extreme Mech. Lett.* **2018**, *21*, 9; e) H. Jin, E. Dong, G. Alici, S. Mao, X. Min, C. Liu, K. H. Low, J. Yang, *Bioinspir. Biomim.* **2016**, *11*, 056012; f) Y. Yang, D. Li, Y. Shen, *IEEE Robot. Autom. Lett.* **2019**, *4*, 1647; g) L. Qin, X. Liang, H. Huang, C. K. Chui, R. C. Yeow, J. Zhu, *Soft Rob.* **2019**, *6*, 455; h) B. Shin, J. Ha, M. Lee, K. Park, G. H. Park, T. H. Choi, K.-J. Cho, H.-Y. Kim, *Sci. Rob.* **2018**, *3*, eaar2629.

[22] J. Brackenbury, *J. Insect Physiol.* **1999**, *45*, 525.

[23] M. D. Ford, J. H. Costello, *Sci. Mar.* **2000**, *64*, 47.

[24] a) S.-W. Yeom, I.-K. Oh, *Smart Mater. Struct.* **2009**, *18*, 085002; b) J. Najem, S. A. Sarles, B. Akle, D. J. Leo, *Smart Mater. Struct.* **2012**, *21*, 094026; c) B. Akle, J. Najem, D. Leo, J. Blottman, Proc. SPIE 7976 Electroactive Polymer Actuators and Devices (EAPAD) **2011**, 797624; d) A. Villanueva, C. Smith, S. Priya, *Bioinspir. Biomim.* **2011**, *6*, 036004; e) S. I. Rich, R. J. Wood, C. Majidi, *Nat. Electron.* **2018**, *1*, 102; f) Y. Tang, J. Yin, *Adv. Mater. Technol.* **2018**, *3*, 1800069.